INT. J. REMOTE SENSING, 2001, VOL. 22, NO. 8, 1495–1520

Gain of the AVHRR visible channel as tracked using bidirectional reflectance of Antarctic and Greenland snow

S. J. MASONIS* and S. G. WARREN

Department of Atmospheric Sciences, University of Washington, Box 351640, Seattle, WA 98195, USA; e-mail: sarahd@atmos.washington.edu

(*Received 28 August 1998; in final form 23 November 1999*)

Abstract. The snow surfaces of the high plateaus of the East Antarctic and Greenland ice sheets are used to determine multi-year drift in the sensitivity of the visible channel of the Advanced Very High Resolution Radiometer (AVHRR) on the polar-orbiting satellites NOAA-9, 10, and 11. Bidirectional reflectance distribution functions are empirically derived for the months of October–February (Antarctica) and April–August (Greenland) using a simplified atmospheric model. The bidirectional reflectance of the snow surface should not change from year to year for near-nadir satellite views. Therefore, drift in the derived bidirectional reflectance distribution function is interpreted as drift in channel sensitivity.

Several factors make the snow surface of an ice sheet suitable as a calibration target for visible and near-UV channels. (1) In this spectral region, snow has a very high albedo ($>97\%$) that is invariant with grain size and incidence angle. (2) On the high plateaus the temperatures are always far below freezing so the surface consists of cold fine-grained snow, and there is negligible contamination. (3) The ice sheet surfaces are uniform and flat across large areas. (4) Ozone is the only significant variable absorber in this spectral region, and its absorption can be accounted for if the ozone amount is known. (5) Cloud detection and removal is not necessary, because the thin clouds over the high ice sheets apparently do not alter the near-nadir reflectance, as they do over dark surfaces.

Our analysis indicates that the visible channel on NOAA-9 degraded linearly over the 3.5-year lifetime of the instrument by $5.3 \pm 0.1\%$ per year. NOAA-10 showed non-linear behaviour that could be fitted with a fourth-order polynomial. Data from NOAA-11 prior to the eruption of Mt Pinatubo showed a linear *increase* in sensitivity of $2.3 \pm 0.2\%$ per year. The derived drifts are not sensitive to the choice of spatial and temporal averaging scales, the choice of months and gridboxes, and whether or not a cloud-rejection scheme is used.

1. AVHRR data description and calibration history

Since July 1981, NOAA satellites of the TIROS-N series have carried Advanced Very High Resolution Radiometer (AVHRR) instruments. The AVHRR is a scanning radiometer with five channels, taking measurements in two solar bands (channel 1, 0.58–0.68 μm and channel 2, 0.73–1.10 μm) and three thermal bands. There are usually two AVHRRs in operation, one with an equator-crossing time in the morning and the other in the afternoon. To date, four morning AVHRRs (on the NOAA-6,

*née Doherty.

International Journal of Remote Sensing
ISSN 0143-1161 print/ISSN 1366-5901 online
http://www.tandf.co.uk/journals

-8, -10, -12 satellites) and four afternoon AVHRRs (on the NOAA-7, -9, -11, -14 satellites) have flown.

This series of AVHRRs has provided a continuous radiance dataset that has been used by many projects, including the International Satellite Cloud Climatology Project (ISCCP) (Rossow and Schiffer 1991) and the Pathfinder project (Ohring and Booth 1995). Climatological parameters such as those being derived by ISCCP and the Pathfinder project will tend to change by small amounts over long periods of time. In order for such small changes to be detected, the AVHRR radiance values must be accurately calibrated over the history of the projects.

The dark noise of the detector, c_0, and a gain factor, g, which convert units of radiance to detector counts, are measured for all AVHRR radiometers prior to launch. However, the initial calibration values do not remain valid for the life of the instrument, as a detector's sensitivity and dark noise often change significantly with time. In addition, when a new AVHRR instrument is launched, inter-satellite calibration must be performed.

Once in orbit, the AVHRR thermal channels are calibrated continuously using on-board, temperature-monitored blackbodies. No such on-board calibration source exists for the two solar channels. Changes in c_0 over time are measured with sufficient accuracy using dark radiances from space. However, monitoring changes in the detector gain, g, is more difficult. It is particularly important to properly calibrate the AVHRR instrument on the NOAA afternoon polar orbiter because radiometers on some geostationary satellites (used by ISCCP) and the AVHRR on the morning polar orbiter are calibrated against the afternoon satellite using co-located images.

Here we present a method for determining the drift in detector gain, dg/dt, for the AVHRR channel 1 using the snow-covered ice sheets of Antarctica and Greenland as targets. For this work we do not use the full-resolution AVHRR data but rather the Reduced Resolution Radiance Data (or 'B3' data) made available by ISCCP (and used by ISCCP for cloud analyses). The B3 data have sufficiently high spatial and temporal resolution for our purposes and are readily available in a convenient format.

In the B3 dataset, the 1 km resolution data are averaged over areas 4–7 km on a side at 30 km intervals every three hours. *Nominal* radiance values have had only the pre-launch calibration conversion factor for counts-to-radiance applied; these are what we use in our analysis. Drift in the NOAA polar orbiter detector calibration constants (g and c_0) are accounted for in the B3 *absolute* calibration dataset.

1.1. *Existing approaches to calibration of the visible channel*

Calibration constants for the AVHRR solar channels have been derived by several groups, mostly using ground-based targets. ISCCP scientists have calibrated channel 1 by a statistical approach that assumes the globally averaged reflectivity for a given scene type (grassland, deciduous forest, land ice, etc.) changes less with time than does the detector response (Brest and Rossow 1992, Rossow *et al.* 1992, 1996, Brest *et al.* 1997). Radiance values from nearly the entire Earth are used.

Other attempts to calibrate channel 1 (and sometimes channel 2 as well) have used desert targets. Staylor (1990), Kaufman and Holben (1993), and Rao and Chen (1995, 1996) used the Libyan Desert, whose albedo is assumed to be stable because of the almost total lack of vegetation. Wu and Zhong (1994) used parts of the Central Asian desert, and Che and Price (1992) used a composite of measurements made by others.

More recently, Loeb (1997) used the Antarctic and Greenland ice sheets to determine changes in both solar channels on the NOAA-11 and NOAA-14 AVHRRs, and Tahnk and Coakley (2001) have successfully applied Loeb's method to obtain improved calibration coefficients for NOAA-14. Jaross (1993) also used ice sheets for calibration at wavelength >340 nm on the Total Ozone Mapping Spectrometer (TOMS). In these studies, all radiances were binned together for a given ice sheet (Antarctic and Greenland), and the calibration change was derived at only a few points in time. The results of these studies suggest that the ice sheets can serve usefully as calibration targets. By making some methodological advances and by calculating the course of calibration drift for nearly every month over several years, we present an even stronger argument for the utility of Antarctica and Greenland as calibration targets.

The calibration drift values dg/dt derived for channel 1 in several previous studies are given in table 1. There are significant disagreements in the derived drifts. Even for NOAA-9, where the agreement is best, the uncertainty is unacceptably large for climatic analyses. For example, if the error in the estimated drift is 1% per year, then over the 4-year life of a satellite the apparent estimates of the Earth's average albedo (0.3) could be in error by 0.012, implying a $4\,\mathrm{Wm}^{-2}$ error in the shortwave Earth radiation budget.

1.2. *Sources of error in existing approaches*

We list what we consider to be the most important sources of error in calibration using ground targets. Some of these apply specifically to desert targets, some to the ISCCP's 'global sites' method, and some to both.

(1) Deserts are fairly red in comparison to the detector response curve for channel 1. If the spectral transmittance of the channel filter changes at its red cutoff, a bias in the absolute calibration is introduced.
(2) Blowing dust may bias the results from desert targets, because the albedo of sand and soil surfaces depends on grain size (Leu 1977), and the average grain size of blowing dust will be smaller than that of the surface. Gradual changes in average winds over several years, as happens with climatological shifts in weather patterns, could therefore introduce calibration errors.
(3) A change in atmospheric loading of sulfate aerosol (such as from European countries for the Libyan Desert) could induce a change in albedo that would appear as a change in detector sensitivity.
(4) The ISCCP calibration method assumes that the seasonal albedo of various

Table 1. Average rate of change in AVHRR channel 1 sensitivity (percent per year), as calculated by different studies.

	NOAA-7	NOAA-9	NOAA-11
Staylor (1990)	−3.5	−6.0	—
Che and Price (1992)	−3.5	−5.0	−6.7
Kaufman and Holben (1993)	−3.8	−5.7	−1.0
Wu and Zhong (1994)	—	−5.8	—
Rao and Chen (1995)	—	−5.9	−1.2
Brest and Rossow (1992)	0	−4.2	—
Brest *et al.* (1997)	−1.1	−5.5	+1.7

land types does not change with time. Although this assumption is better than simply assuming the average albedo of the planet is constant, it can lead to error because climate change is expected to lead to vegetation changes.

(5) All of the mentioned studies require cloud detection and removal methods. High, thin, spatially uniform clouds are particularly difficult to detect. A change in the frequency of this type of cloud could cause incorrect calibration drifts to be inferred.

(6) The azimuth angle between the Sun and the satellite changes with time for all the NOAA polar orbiters, leading to a corresponding shift in average solar and satellite zenith angles for a specific location's radiance measurements. None of the Earth's surfaces are isotropic reflectors, so changes in the Sun/satellite azimuth will induce a shift in the inferred albedo. Brest *et al.* (1997) corrected for this effect when performing inter-satellite calibration, using an empirical correction derived from NOAA-7 data. However, they were not confident enough in this method to apply it to the long-term drift correction. Therefore, an unquantified portion of the change in inferred albedo attributed to calibration drift is in fact caused by changing solar and satellite zenith angles.

2. Snow-covered ice sheet surfaces as visible-channel calibration targets

As pointed out by Loeb (1997), the snow-covered surfaces of the Antarctic and Greenland high plateaus offer advantages over desert sites for calibration of the AVHRR visible channel. This is principally because there are fewer sources of variability in the surface albedo and bidirectional reflectance. At visible wavelengths, snow surfaces have a high albedo that is invariant with grain size. Figure 1(*a*) from Grenfell *et al.* (1994) shows that the snow surface albedo in Antarctica is in the range 0.96–0.99 from 300 to 700 nm wavelength. Near-infrared albedo varied over the course of two months at South Pole Station in 1986 and one month in 1991 as the snow surface aged, drifted, and was renewed by falling snow or surface frost, but the visible and near-UV albedo remained constant. The same constant values were also found by Grenfell *et al.* (1994) at Vostok Station, 1300 km away. The visible albedo of the snow surface of the Antarctica plateau is therefore very reliable. Modelling studies also show that snow grain growth with time should not affect the visible albedo as long as there is no melting (Wiscombe and Warren 1980). In addition, unlike blowing dust over a desert, blowing snow will not affect the albedo of the ice sheets in channel 1 because snow is non-absorbing at visible wavelengths. On surfaces with sastrugi (centimetre-to-metre-scale snow dunes), blowing snow may hide shadowed and highlighted sastrugi faces, affecting the bidirectional reflectance (Warren *et al.* 1998). Averaging over spatial scales several orders of magnitude larger than the scale of the surface feature will reduce this type of error only if the sastrugi orientation is not constant over the large area. We therefore reduce this error by selecting regions with less prominent sastrugi and selecting a restricted range of viewing angles where the bidirectional reflectance is less sensitive to sastrugi. With these restrictions, the interannual variability of the bidirectional reflectance distribution function for a given time of year and at a given location in East Antarctica or North Greenland should be very low.

A significant advantage of the cold snow surface calibration target over all other targets is that a procedure for detection and elimination of clouds appears not to be

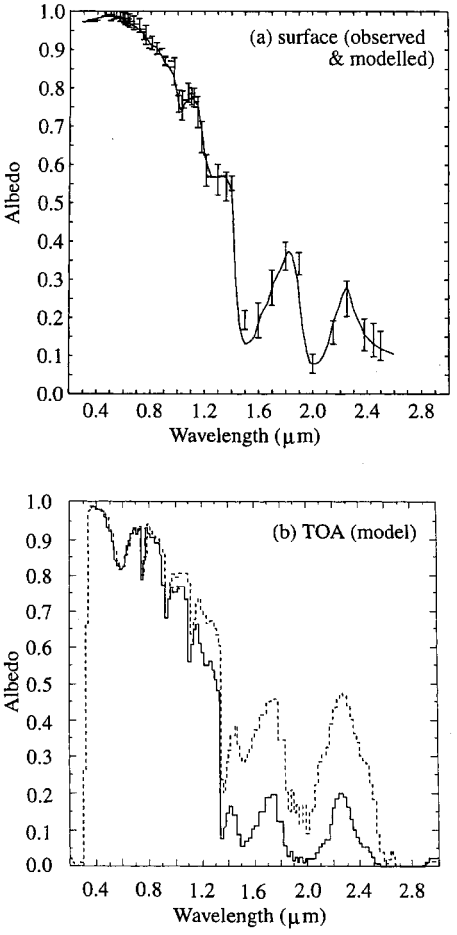

Figure 1. (*a*) Measured (with error bars) and modelled spectral albedo of Antarctic snow, from Grenfell *et al.* (1994, figure 4). (*b*) Spectral albedo at the top of the atmosphere, from radiative-transfer model calculations, over Plateau Station (79° S) with solar zenith angle 66° for a clear sky (solid line) and with a cirrostratus cloud at 1.0–2.7 km height (3.7 particles/cm^3, effective radius = 15.6 μm, dashed line). A January temperature profile is used with 100% relative humidity (with respect to ice) in the troposphere. The near-IR albedo is higher when the cloud is present, but the visible albedo is unchanged (Warren and Wiscombe 1980, unpublished results). The model is described by Wiscombe *et al.* (1984). The dip in albedo at wavelength 0.6 μm is due to absorption by ozone.

needed. Clouds, like the underlying snow surface, are non-absorbing at visible wavelengths, so a uniform cloud will simply add another scattering layer. The albedo of snow is so high that this additional scattering layer should not affect the overall planetary albedo at visible wavelengths, although the near-IR albedo will be affected (figure 1(*b*)). Bright spots do appear where cloud edges face incident sunlight, and dark regions will appear where the satellite views a snow surface in the shadow of a cloud. Statistical filtering can be used to minimize these effects of clouds if necessary. However, we show that the derived calibration drift, when calculated using radiances

only from near-nadir views, is the same whether or not statistical cloud-removal procedures are applied.

Unlike over the desert targets, there are no significant sources of tropospheric aerosols to alter the planetary albedo over the Antarctic Plateau. Our derived drifts in bidirectional reflectance for Greenland and Antarctica are in good agreement, indicating that year-to-year variation in Arctic haze is not significantly affecting the Greenland results.

The reflectance of snow is uniformly high over the full range of wavelengths measured by the AVHRR channel 1, providing a target that is more spectrally uniform than the reddish desert targets. Finally, the Antarctic and Greenland plateaus do not present political impediments to the conduct of field measurements to investigate the surface targets (Grenfell *et al.* 1994, Warren *et al.* 1998).

The analysis procedure developed herein for the NOAA-9, -10 and -11 AVHRRs could also be applied to AVHRR instruments on other satellites, as well as to other visible or near-UV channels on polar orbiting satellites. It is possible to use this method for near-UV channels because, as in the visible, the UV albedo of snow is high and invariant with grain size (Grenfell *et al.* 1994, figure 5), and likewise clouds are non-absorptive in the UV.

3. Model of radiative transfer over an ice sheet

Our method is designed to obtain the calibration drift, dg/dt, but not the absolute value of g as a function of time t. Our method involves inferring a bidirectional reflectance function ρ at time t and comparing it to $\rho(t_0)$, where t_0 is an arbitrary time during the lifetime of the satellite. Only the ratio $\rho(t)/\rho(t_0)$ is needed to obtain the drift.

The factors affecting the radiance I ($\mathrm{Wm^{-2}sr^{-1}}$) received by the satellite are (1) the solar irradiance $S\cos\theta_s$, (2) Chappuis band absorption by the ozone path length m (the sum of the upward and downward paths), which permits a fraction $t(m)$ of the incident radiation to be transmitted, and (3) the angular pattern of reflectance by clouds and snow (including Rayleigh scattering), given by ρ (figure 2):

$$I = S\cos\theta_s t(m)\rho(\theta_s, \theta_r, \phi) \tag{1}$$

where S is the solar irradiance, θ_s is the zenith angle of the Sun relative to the surface, θ_r the zenith angle of reflected light, as viewed by the satellite, and ϕ the relative azimuth angle between the Sun and the satellite.

Our model consists of this simple equation, which was also used by Boime and Warren (1993). It assumes that all the scattering occurs below the ozone layer; this is what allows the single equation (1) to be used in place of a complex radiative transfer model. Potential sources of error resulting from this assumption are discussed in §4.1.3.

We now discuss each of the three terms in (1).

3.1. *Solar irradiance*

The incident irradiance at the top of the atmosphere (TOA) in channel 1, perpendicular to the solar beam, is

$$S = \int S_\lambda w(\lambda) d\lambda \tag{2}$$

where λ is wavelength, S_λ is the extraterrestrial solar spectrum for the Earth-Sun

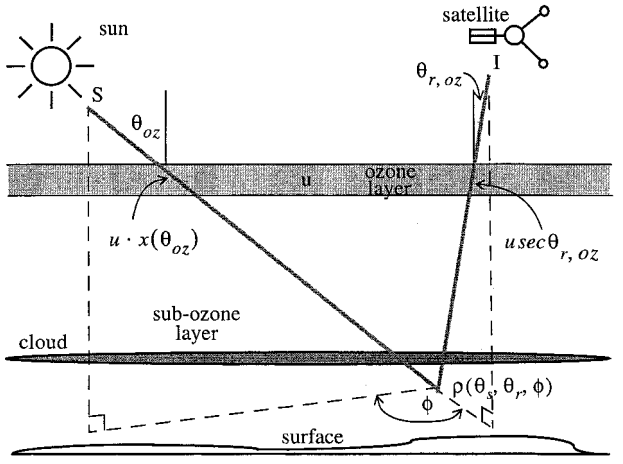

Figure 2. A diagram to illustrate the components of equation (1).

distance on a given day, and $w(\lambda)$ is the normalized channel sensitivity function for channel 1.

The angle of incidence on the surface, θ_s, is the same as the solar zenith angle θ_0 if the surface is horizontal, but in general for a surface of slope γ, θ_s is determined from the formula given by Dozier and Frew (1989) as

$$\cos\theta_s = \cos\gamma\cos\theta_0 + \sin\gamma\sin\theta_0\cos(\phi_0 - \alpha) \tag{3}$$

where α is the slope azimuth east of north and ϕ_0 is the solar azimuth east of north.

3.2. *Absorption by ozone*

The two-way transmittance $t(m)$ through the ozone layer is a function of the ozone path length m:

$$m = u[\sec\theta_{r,oz} + x(\theta_{oz})] \tag{4}$$

where u is the total column amount of ozone, θ_{oz} is the solar zenith angle at the ozone layer, and $\theta_{r,oz}$ is the reflectance zenith angle at the ozone layer. Because of the Earth's curvature, $\theta_{oz} < \theta_0$; this is accounted for in our model. However, $\theta_{r,oz} \approx \theta_r$ because we only use radiances with $\theta_r \leqslant 18°$, as explained below. The atmospheric pathlength function $x(\theta)$ must also account for Earth's curvature; for small θ, $x(\theta) \approx \sec\theta$.

The transmittance $t(m)$ is determined as an integral over the Chappuis absorption band of ozone, weighted by S_λ and $w(\lambda)$:

$$t(m) = \frac{\int S_\lambda w(\lambda) e^{-k(\lambda)m} d\lambda}{\int S_\lambda w(\lambda) d\lambda} \tag{5}$$

There is a very substantial overlap of the spectral absorption coefficient, $k(\lambda)$, with $w(\lambda)$, because Chappuis band absorption is strong between 575 and 675 nm. It is therefore important to account accurately for day-to-day variations in ozone amount. The coefficient $k(\lambda)$ is given by Anderson and Mauersberger (1992), whose laboratory measurements are in excellent agreement with the earlier measurements of Vigroux (1953). Equation 5 was used to create a table of values of t over a large range of m,

and a sixth order polynomial fit of log t versus m is used in our analyses. The function must be recalculated for each satellite, as the shape of $w(\lambda)$ changes.

Other researchers using ground targets for absolute calibration of AVHRR channel 1 have used zonally averaged or climatological mean ozone amounts to calculate loss due to Chappuis absorption. However, a deviation from climatology in the local column ozone amount at the time of a calibration measurement can result in significiant errors in the calculation of expected upwelling radiance. Over Antarctica in particular, the opening and closing of the springtime 'ozone hole' causes rapid, large changes in ozone. We therefore use daily values of total column ozone from TOMS to calculate m. Errors in the derived drift due to uncertainty in column ozone amount are reduced by using only near-nadir views, minimizing the ozone path length.

3.3. *Reflection by snow and atmospheric components*

Determination of the fraction of sunlight scattered in the direction of the detector by constituents of the Earth/atmosphere system presents the greatest difficulty, by far, in calculating the expected amount of radiation reaching the satellite. In most calibration studies to date using ground targets, a radiative transfer model was used to calculate atmospheric losses from molecular Rayleigh scattering and from scattering by aerosols. Models are also used to account for the effects of changes in θ_0, θ_r and ϕ on reflected intensity, known as the 'bidirectional effect'. In (1) we have replaced the use of a radiative transfer model with a simplified parameterization of incident sunlight's interaction with the Earth/atmosphere system.

The surface (or 'sub-ozone layer') reflects a fraction A_s of the incident sunlight. The surface albedo A_s for Antarctic snow (figure 1(*a*)) has been measured as 0.97 at the wavelengths of channel 1; it is so high that the albedo of the entire sub-ozone layer, including clouds (which are essentially non-absorbing) and Rayleigh scatter, cannot be significantly different from this. The albedo of snow does increase with angle of incidence θ_s at wavelengths where there is significant absorption, but it is independent of θ_s in the visible and near-UV for grain radii smaller than 200 μm, typical of cold snow (Wiscombe and Warren 1980, figure 8). The albedo of clouds over dark surfaces normally depends on zenith angle even at visible wavelengths because clouds have finite optical thickness (unlike snow, which is semi-infinite), but the combined cloud-snow system is a semi-infinite medium, so like snow its albedo at visible wavelengths is independent of θ_s. The albedo even for zenith Sun is so high (~ 0.97) that it cannot increase much as the Sun drops lower in the sky.

If the sub-ozone layer were to scatter light isotropically into the upward hemisphere, the reflected radiance would just be the reflected irradiance divided by π. Deviations from isotropic reflectance are accounted for by the anisotropic reflectance factor $R(\theta_s, \theta_r, \phi)$ (Suttles *et al.* 1988); the three factors A_s, π, and R combine to make the bidirectional reflectance ρ (units sr^{-1}), which appears in (1), as

$$\rho(\theta_s, \theta_r, \phi) = \frac{A_s}{\pi} R(\theta_s, \theta_r, \phi) \tag{6}$$

R has the property that its average value over the upward hemisphere (weighted by its contribution to the upward irradiance, proportional to $\cos\theta_r$) is unity:

$$\bar{R} = \frac{1}{\pi} \int_0^{2\pi} \int_0^{\pi/2} R(\theta_s, \theta_r, \phi) \cos\theta_r \sin\theta_r \, d\theta_r \, d\phi = 1 \tag{7}$$

By representing R (and ρ) as a function of only three angles we are ignoring the additional dependence of R on the azimuth angle between the Sun and the wind. This dependence can be significant, as shown by Warren *et al.* (1998, figure 5). However, as also shown by Warren *et al.* and verified below, the sastrugi have almost no effect on reflectances into near-vertical directions, as employed in this study.

3.4. *Solution of equation (1)*

For each reported satellite radiance, I, given in the B3 nominally calibrated dataset, we determine the corresponding values of S, θ_s, and m and solve for the product $A_s R$ (or $\pi\rho$), which we call χ:

$$\chi(\theta_s, \theta_r, \phi) = \frac{\pi I}{S \cos\theta_s t(m)} \tag{8}$$

In our calibration approach, we allow for the possibility that χ may vary seasonally and geographically (due principally to variations in sastrugi), but that for a particular location in a particular month it does not vary interannually. Any year-to-year variation in χ we therefore interpret as drift in the channel sensitivity g. A climatological change in the sub-ozone cloud amount should not cause a systematic bias in $\chi(\theta_s, \theta_r, \phi)$ over snow-covered surfaces, though it may add noise.

The angles $(\theta_0, \theta_r, \phi)$ are given in the B3 radiance dataset along with each radiance I. The daily value of column ozone amount u is obtained for each location from the TOMS Version 7 dataset; m is then computed using the known angles.

For the afternoon satellites (NOAA-9 and -11), the value of ϕ is close to 35° when the satellite is looking away from the Sun (and thus sees 'backward scattered' radiation) and 145° when looking toward the Sun (so it sees 'forward scattered' radiation). For the morning satellites, these angles are 20° and 160°. The equator-crossing time for a given satellite drifts over the lifetime of the satellite, causing the two values of ϕ to drift; the effect of this orbital precession on our model are discussed later.

Surface slope and azimuth on the Antarctic Plateau were obtained from J. L. Bamber (personal communication). They were generated using elevations derived from ERS-1 altimeter data, at 10 km × 10 km horizontal resolution (Bamber 1994). We did not account for non-zero surface slope in Greenland. However, we did restrict our Greenland analysis to regions of low slope and high elevation (> 2 km), as determined from a USGS map.

4. Bidirectional reflectance functions

4.1. *Sources of error*

4.1.1. *Variability of surface slope*

The horizontal resolution of the radiance data is finer than the resolution of the Antarctic slope data (10 km × 10 km) used in the model, so slopes varying on scales between 4 and 10 km can cause inaccuracy in our calculation of θ_s. Seko *et al.* (1993) inferred a direct correlation between average surface slope and variability of surface slope in their analysis of AVHRR channel 1 radiances over Antarctica, which they linked to snow surface features of width 5–25 km. They found that the undulations at higher altitudes on the Plateau have longer wavelength and smaller amplitude. Above 2 km elevation, the average wavelength of these features is > 10 km. Thus, we have restricted our analyses to areas at or above 2 km in elevation, where large-scale surface undulations can be at least partially resolved in our slope dataset. This

restriction also prevents the inclusion of radiances from the low-elevation ice shelves, which are flat but can experience melting in the summertime.

On a much smaller scale, ~1 m wide sastrugi may also add error to χ for a given location, particularly because the azimuth angle between the Sun and sastrugi orientation changes from one satellite pass to the next (Warren *et al.* 1998). Sastrugi size and orientation are dictated by prevailing winds, which on the high plateau are intimately linked to topography. Katabatic winds carry cold air along the surface, from the high plateau towards the coast, and are consistent in speed and direction for a given location and time of year. Steeper areas have strong surface winds, which build large sastrugi (Parish and Bromwich 1987). We therefore restrict the Antarctic analyses to regions with slope <0.006 radians (at 10 km resolution) (figure 3(*a*)). This also ensures that all mountainous regions are avoided.

4.1.2. *Cloud edges and shadowing*

As noted earlier, non-absorbing, flat-topped cloud layers over the snow surface should not increase the albedo of the sub-ozone layer at visible wavelengths, but uneven cloud tops and cloud edges may introduce noise into our empirical determination of χ. Effects of rough cloud tops should be small because convective clouds are rare over the high ice sheet plateaus. Most clouds in these regions are stratiform (Warren *et al.* 1986), so the main concerns are cloud shadows and bright spots where cloud edges face incident Sunlight.

We tested the effects of viewing cloud edges and shadows by deriving χ both with and without a 'cloud-edge rejection' procedure. The procedure was simply to exclude anomalously high and low radiances in the calculation of χ. Our derived calibration drift for the NOAA-9 AVHRR was the same in both cases, and, as shown

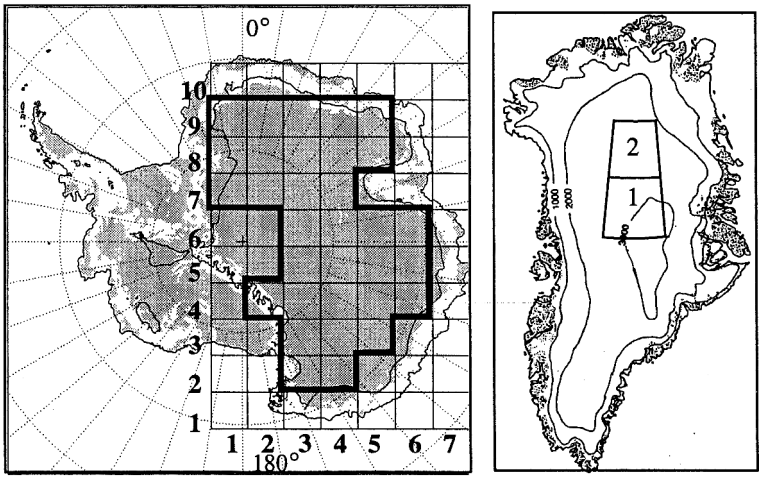

Figure 3. (*a*) Regions of the Antarctic continent with slope <0.006 radians (0.34°) at 10 km resolution (shaded), with the height contour for 2000 m superimposed. The 32 gridboxes (~444 km on a side) for which individual monthly plots of χ_n are generated are outlined. (*b*) The two gridboxes on the Greenland high plateau used in this study. Both gridboxes are bounded by longitudes 35° and 45° W; the latitudes spanned are 72–75° N for gridbox 1 and 75–78° N for gridbox 2. The two maps are on different scales.

in table 2, there also was no significant decrease in the noise in χ when the cloud-edge rejection procedure was applied. From this we conclude that cloud detection and elimination is not necessary for determination of calibration drift over the snow-covered plateaus at visible and near-ultraviolet wavelengths.

4.1.3. *Scattering within and above the ozone layer*

Incident light that is scattered above or within the ozone layer is not attenuated by Chappuis band absorption as much as is assumed by the model, so the derived value of χ for the 'sub-ozone layer' will be somewhat greater than the true value. Scattering sources in and above the ozone layer include air molecules, stratospheric aerosols, and, in a restricted set of regions and months, polar stratospheric clouds (PSCs).

The amount of Rayleigh scattering above the sub-ozone layer is proportional to the atmospheric pressure at the top of this layer and is also approximately proportional to $\sec\theta_0$. For a given time of year and for a given θ_0 and θ_r, Rayleigh scattering by air molecules within and above the ozone layer should not vary much from one year to the next, because the average height of the ozone layer should not deviate significantly from climatology. Thus, although our derived value of χ will be slightly inaccurate, the introduced bias should not change interannually, so our calculation of channel 1 drift should not be affected.

Polar stratospheric clouds occur only in the winter and early spring, residing between 10 km and 25 km altitude, coincident with the ozone layer (Poole and Pitts 1994). Temperatures low enough for PSC formation rarely occur outside of the months of June through October in Antarctica (Poole and Pitts 1994) and occur only fleetingly over Greenland. October is therefore the only month used in our calculations in which PSCs might affect our derivation of calibration drift.

Stratospheric aerosols, like PSCs, also occupy the ozone layer. In most years, stratospheric aerosol concentrations are small enough that their effect is negligible. However, major volcanic eruptions result in significant stratospheric sulfate loads that last for several years. Aerosol above the ozone layer can cause reduced Chappuis absorption because some of the sunlight is scattered up before it encounters ozone; aerosol within the ozone layer may cause increased absorption by lengthening the paths of photons through the layer. Stratospheric aerosols not only directly affect the planetary albedo but also act as cloud condensation nuclei. An increase in the probability of polar stratospheric cloud formation has been seen in the presence of

Table 2. Angular average geographic variability $\sigma_{g,a}$ of χ_n. The standard deviation is taken over 32 geographic gridboxes on the East Antarctic Plateau for 1985–1986 NOAA-9 data. The calculation of χ_n used either: (*a*) the mean of all derived χ values; (*b*) the mean of the middle 60% of all derived χ values, if the standard deviation of the distribution was greater than 0.03, otherwise same as (*a*); or (*c*) the median of all derived χ values (shown also as '○' in figure 7).

	Averaged over all angular bins					Average over bins with $\mu \geqslant 0.95$ and $\mu_s \geqslant 0.10$				
Method	Oct.	Nov.	Dec.	Jan.	Feb.	Oct.	Nov.	Dec.	Jan.	Feb.
a	0.0345	0.0310	0.0235	0.0245	0.0262	0.0214	0.0164	0.0161	0.0217	0.0193
b	0.0352	0.0315	0.0233	0.0222	0.0270	0.0209	0.0151	0.0126	0.0156	0.0203
c	0.0358	0.0318	0.0239	0.0222	0.0275	0.0210	0.0145	0.0120	0.0148	0.0197

volcanic aerosols during months when temperatures are cold enough for PSC formation (McCormick and Trepte 1987, Deshler *et al.* 1994). Because our model does not account for stratospheric aerosols, it is not useful at times when stratospheric aerosol loading is large. As we will see below, our computed drifts are unreliable in 1992 because of Pinatubo aerosol.

The errors discussed in this section affect only channels with significant ozone absorption (i.e. near 600 nm). Radiances from snow surfaces in other visible and near-UV channels should be unaffected by variations in stratospheric aerosols, PSCs, and the height of the ozone layer.

4.1.4. *Use of overhead total column ozone amount*

The total column ozone (u), that we use in (4) is the value given by TOMS for directly above the ground target. The ozone on the upward path is very close (horizontally) to the ground target, because we only use data with $\theta_r \leqslant 18^\circ$. However, on the downward path, when the Sun is low, the solar beam passes through the ozone layer some horizontal distance away from the ground target, where u may be different. This could be accounted for in the analyses, but we have not done so. Its effect would be greatest in the Antarctic spring, when the horizontal gradient of u and the solar zenith angle are both large.

4.2. *Generation of bidirectional reflectance plots*

Noise in our derived bidirectional reflectance functions is reduced by statistical processing. Values of $\chi(\theta_s, \theta_r, \phi)$ derived for a given month, year, and geographic gridbox are binned in angular space. Bins are classified by ranges of μ_s and μ_r, where $\mu_s = \cos\theta_s$ and $\mu_r = \cos\theta_r$, and are 0.01×0.01 in size. Each plotted χ function has two 'halves', corresponding to foward-scattered and backward-scattered light (i.e. $\phi \approx 35^\circ$ and $\phi \approx 145^\circ$, respectively, for afternoon satellites and $\phi \approx 20^\circ$ and $\phi \approx 160^\circ$ for morning satellites). For each angular bin, the plotted value of χ is either an average over, or the median of, a number (n) of individual derived values, which we designate as χ_n.

Three methods for calculating $\chi_n(\theta_s, \theta_r, \phi)$ were tested to determine how best to minimize noise (presumably due to cloud edges) in χ_n and in our calculated calibration drift: (a) the mean of all derived values of $\chi(\theta_s, \theta_r, \phi)$; (b) the mean of the middle 60% of the derived values, if the standard deviation of the distribution is greater than 0.03; otherwise the mean of all values; (c) the median of all derived values. The effectiveness of each of these approaches in reducing noise in χ_n functions is discussed in §4.4, and the effect on calculated calibration drift is discussed in §5.2. We will end up concluding that it does not matter much which method is used, but we favour method (c).

The bidirectional reflectance distribution function for a snow surface should vary smoothly with angle. Derived values of χ_n can therefore be used to generate interpolated values for bins in angular space than do not have a derived value but that are within the domain of (θ_s, θ_r) space containing derived values. Even after the statistical filtering used to generate individual values of $\chi_n(\theta_s, \theta_r, \phi)$, plots of χ show some unnaturally rapid, random variations with θ_s and θ_r. This residual noise is reduced by smoothing the plots over (θ_s, θ_r) space.

In smoothing the χ function, it is essential that real variations in χ not be lost. Therefore, we first divide the noisy plot of χ_n by an empirically-derived function f before smoothing, where

$$f \equiv \frac{(1.1 + \mu_s)}{(\mu_s^{0.6} + \mu_r^{0.6})} \tag{9}$$

The shape of f was chosen to approximate that of χ, so χ_n/f is a 'flattened' version of the original. The flattened plot is then smoothed using a normalized Gaussian-weighted shifting window 5×5 bins in size. The resulting smoothed plot is then multiplied by the function f to produce the smoothed plot of χ_n (figure 4). The individual steps in this procedure are displayed by Doherty (1997).

4.3. *Selection of spatial and temporal scales for derivation of* χ_n

Individual values of $\chi_n(\theta_s, \theta_r, \phi)$ were generated using a month of radiances taken over a broad geographical area. Since sastrugi height and orientation will certainly change from one area to the next, it is important to limit the geographic area covered by a single χ_n function. Because sastrugi orientation is determined by the prevailing katabatic wind direction, the orientation of the sastrugi for a given region and month should not change significantly from one year to the next. Sastrugi size does however, change with season, so individual χ_n functions should also cover a restricted time scale; we use one-month intervals. The need to limit the spatial and temporal scale covered by individual χ_n functions because of geographic and seasonal variability in the snow surface must be balanced against the need for a sufficient number of radiance measurements to reduce the sampling error and also the need to obtain views over a large range of angles.

The reason for needing a large range of viewing angles is that to determine calibration drift we calculate an average χ_n over a fixed subset of angular bins

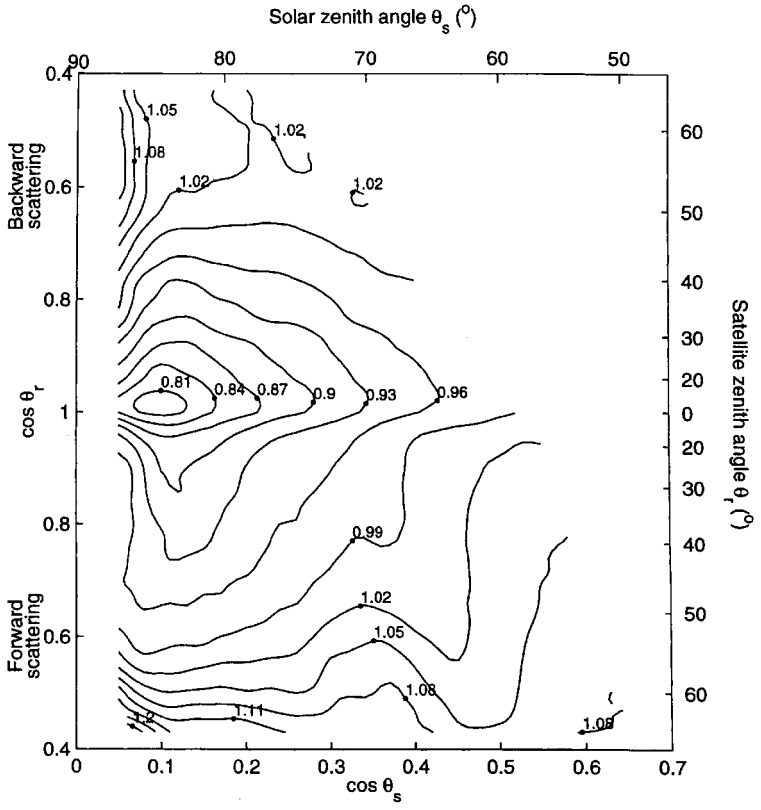

Figure 4. Empirically derived χ function for January 1986 for the East Antarctic plateau.

(i.e. $\chi_{n,a}$, where a = 'angles') for each month. For a given satellite and a given month, the average must be taken over the same subset of angular bins every year to avoid bias due to 'bidirectional effects'. Because the satellite has approximately the same equator-crossing time for each day of the month in a given year, only a restricted area in (μ_s, μ_r) space will be covered for a specific ground location. However, from one year to the next, orbital degradation can lead to a significant shift in the (μ_s, μ_r) space covered for a given month and location. Individual plots of χ_n must have enough coverage in (μ_s, μ_r) space that there are overlapping data for all years in the lifetime of the satellite. To balance the need for limited spatial coverage against the need for good statistics, we chose to use gridboxes 4° of arc on a side ($\sim$444 km × 444 km) in Antarctica (figure 3(*a*)). For Greenland we chose to use two somewhat smaller gridboxes high on the ice sheet (figure 3(*b*)) which do not experience melting, even during summer months (Bader 1961), and which are relatively flat.

4.4. *Geographic variability of χ for Antarctica*

The geographic variability (σ_g) of χ_n for a given month and year is calculated as $\sigma_g \equiv \sigma(R_n)$, where the calculation is taken over all 32 Antarctic gridboxes for each angular bin. Contour plots of the monthly averaged geographic variability for NOAA-9 in October and December 1986, are shown in figures 5 and 6; results for

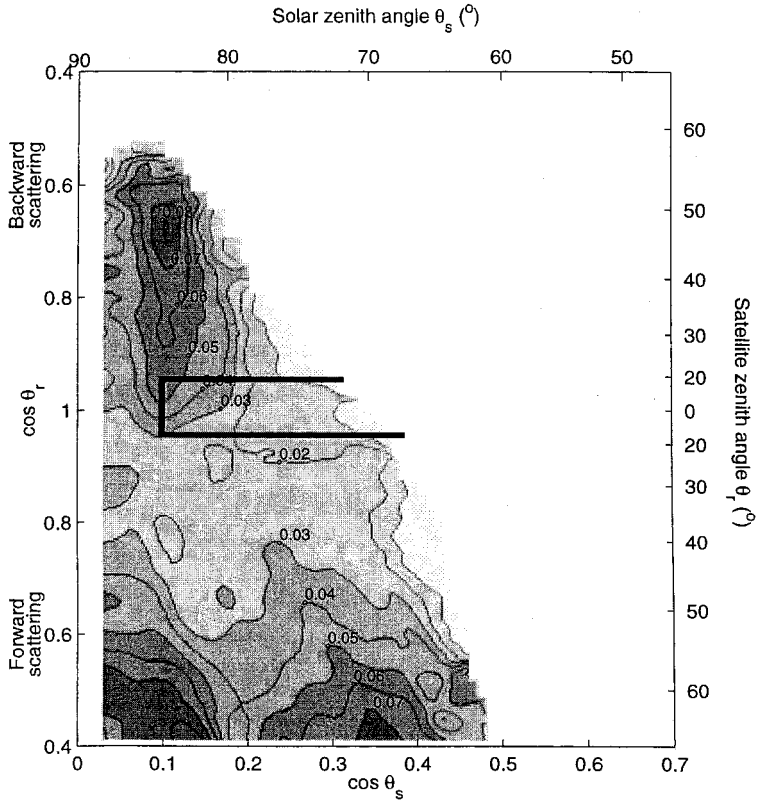

Figure 5. Geographic variability σ_g in χ for October 1986, where the standard deviation is taken over the 32 Antarctic gridboxes outlined in figure 3(*a*). The region with $\mu_r \geqslant 0.95$ and $\mu_s \geqslant 0.10$ is outlined.

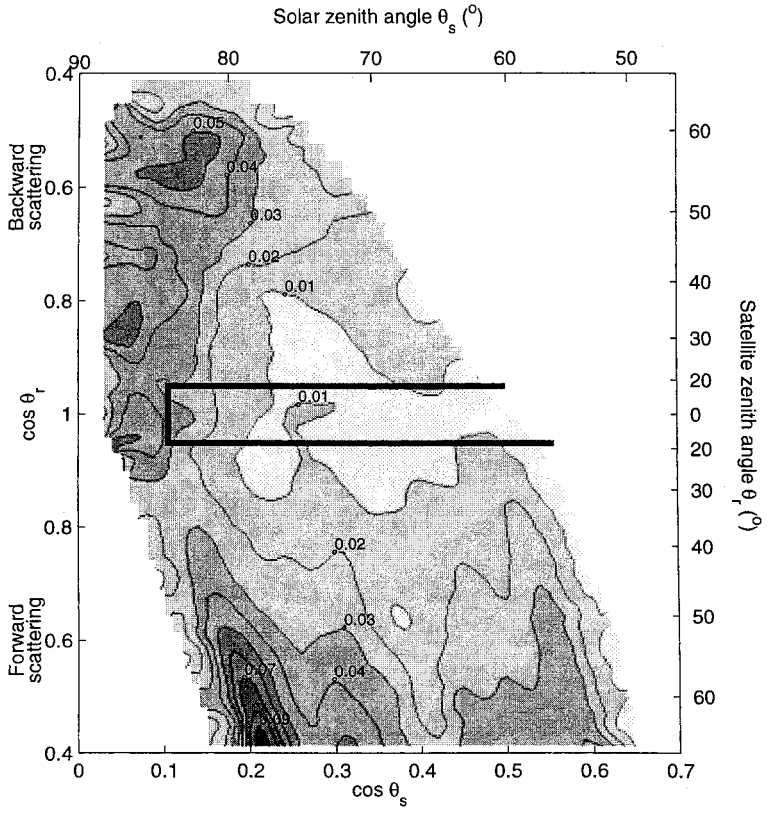

Figure 6. Geographic variability σ_g in χ for December 1986, where the standard deviation is taken over the 32 Antarctic gridboxes outlined in figure 3(*a*). The region with $\mu_r \geqslant 0.95$ and $\mu_s \geqslant 0.10$ is outlined.

other months are given by Doherty (1997). Geographic variability was calculated for the months October to February for all years in which NOAA-9 was operational; the angular average of σ_g is shown in figure 7.

Figures 5 and 6 show that σ_g is generally lowest for near-nadir viewing angles and for smaller solar zenith angles. This is to be expected because $I \propto \cos\theta_s$ and $\partial \cos\theta_s / \partial\theta_s$ is larger at large θ_s, so it is sensitive to error in surface slope. Also, shadowing and bright spots from sastrugi will have a bigger effect at large solar zenith angles (Warren *et al.* 1998). Figures 5 and 6 also show that χ is less variable in the forward-scattering direction than in the backscattering direction for near-nadir views, in agreement with the observations of Warren *et al.* (1998). Figure 7 shows that December has the lowest geographic variability. This is partly because of the smaller solar zenith angles. However, even for the same regions in (μ_s, μ_r) space, χ is less variable in mid-summer than in spring and autumn. This is probably because sastrugi are less prominent in summer, because of weaker winds and 'deflation' due to solar radiation and sublimation, as explained by Gow (1965).

The χ-plots in figures 5 and 6 were produced using the median to obtain χ_n (method (c) in §4.2). We also computed σ_g for plots that had been generated using the two other statistical methods for calculating χ_n. There is very little difference in σ_g amongst the three methods (table 2), but the 'median' method (c) produces slightly

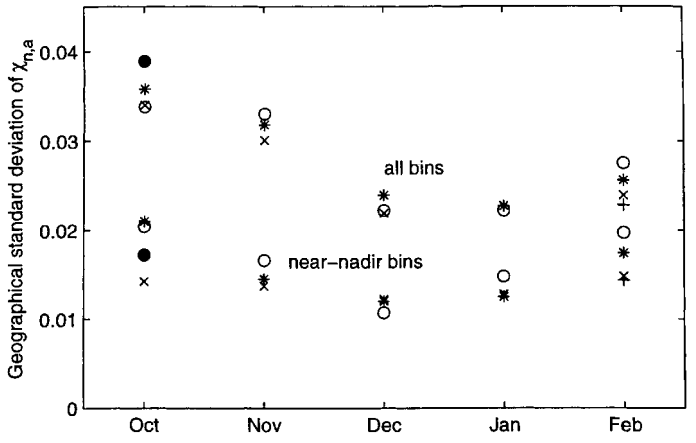

Figure 7. Angular average of geographic variability, $\sigma_{g,a}$, among 32 Antarctic gridboxes for the seasons 1984–85 (+), 1985–86 (○), 1986–87 (1), 1987–88 (×) and 1988–89 (●). In the upper series, the average is taken over all angular bins in that month and year's χ function. In the lower series it is taken only over angular bins with $\mu_s \geqslant 0.10$ and $\mu_r \geqslant 0.95$, as outlined in figures 5 and 6.

lower geographic variability for the near-nadir bins. This is therefore the method we used for determination of calibration drift.

5. Calibration drift

5.1. *Biases in the calculation*

Drift in the Sun/satellite azimuth angle, ϕ, due to orbital degradation (figure 8) can potentially introduce a bias into our model's derived values of χ_n, because χ values are binned only into two angular bins of ϕ in our procedure: 'forward scattered' and 'backward scattered'.

This bias can be assessed using a parameterization of the angular dependence of $R(\theta_s, \theta_r, \phi)$ given in Warren *et al.* (1988), using ground-based measurements at the

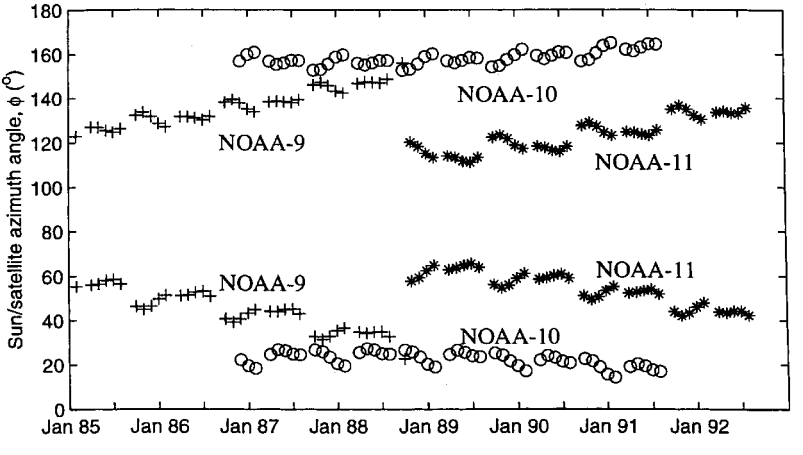

Figure 8. Monthly average Sun/satellite azimuth angle (ϕ) for the radiances used to calculate χ_n. Average angles for April–August apply to Greenland; those for October–February apply to Antarctica.

South Pole. For near-nadir views ($\mu \geqslant 0.95$), χ is nearly independent of ϕ. Averaging R over the angles $60^\circ \leqslant \theta_0 \leqslant 85^\circ$ and $0^\circ \leqslant \theta_r \leqslant 18^\circ$, and over both forward- and back-scattered contributions, this parameterization gives an expected increase in R, and thus in $\chi_{n,a}$, of only 0.06% per year for both NOAA-9 and -11, given their respective changes in ϕ. The azimuth angle for NOAA-10 changed much less over its lifetime than for the other two satellites and the effect on $\chi_{n,a}$ is insignificant.

A second effect of orbital degradation is that the Sun and satellite azimuths relative to sastrugi orientation will shift as the satellite's equator-crossing time changes, leading to interannual changes in the χ_n for a given month and gridbox. Our use of near-nadir views and low-slope target regions minimizes the effect of sastrugi, as noted above. Also, bias in χ_n due to changing Sun/sastrugi azimuth is likely to be different in different geographic gridboxes, so propagation of this error can be minimized by calculating an average drift over many gridboxes.

5.2. *Method used to calculate calibration drift, drift uncertainty, and detrended standard deviation*

We first calculate $\chi_{n,a}$, where the subscript 'n' denotes taking the median of the χ distribution for a given geographic gridbox, month, and angular bin to get χ_n, and the subscript 'a' denotes an angular average of χ_n over a restricted range of (μ_s, μ_r) space. For each gridbox, we plot $\chi_{n,a}$ versus time, then generate a separate least squares linear or polynomial fit to the multi-year data for each month (figure 9(*a*)). For NOAA-11 we terminate the linear fit at July 1991 because subsequent months were affected by Pinatubo aerosols.

The fits in figure 9(*a*) are offset from one another principally because different angular bins were used for different months of the year, according to the solar and satellite zenith angles experienced in different months, but also because of seasonal variability in χ. To separate seasonal variability and bidirectional effects from calibration drift, we multiply each month's fitted line by a factor that forces the lines for all months to intersect at one arbitrary normalization date, chosen as January 1986 for NOAA-9, November 1988 for NOAA-10, and January 1990 for NOAA-11. January 1986 was used as the NOAA-9 anchor point for consistency with the work done by Staylor (1990), but the selection of anchor point does not affect the derived value of calibration drift, dg/dt. A single linear or polynomial fit is then generated for the merged dataset of all months (figures 9(*b*), 10, and 11), where we have also accounted for the change in Sun/satellite azimuth angle over the calibration period (§5.1). The detrended standard deviation, σ_d, is also calculated.

Figures 9, 10 and 11 are for just one Antarctic gridbox paired with one Greenland gridbox. Such estimates are obtained independently for each of the 32 Antarctic boxes paired alternately with the 2 Greenland boxes. We then compute the uncertainty in dg/dt for NOAA-9 and 11 as the standard deviation of the slopes of the fitted lines of all 64 gridbox combinations. The uncertainty in the NOAA-10 calibration change is calculated as the standard deviation of each of the five coefficients to the fourth order polynomial fit, again across all 64 gridbox combinations.

The method described above was applied to data selected with three different choices for the maximum allowed solar zenith angle: 84.3°, 81.4°, or 78.5° ($\mu_s = 0.10$, 0.15, or 0.20). For the more restrictive choices, not all of the 32 Antarctic gridboxes had sufficient data for all months. For $\mu_s \geqslant 0.25$ none of the Antarctic gridboxes have data for all months.

We combine the results from different gridboxes into an estimate of calibration

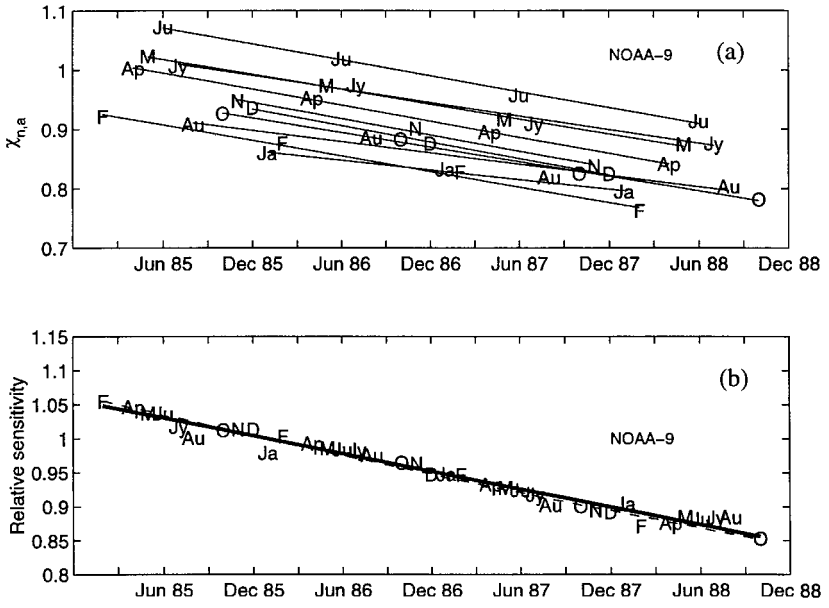

Figure 9. An example of the procedure used to calculate interannual calibration drift and variability. Shown are data for the Antarctic gridbox (4,4) and the Greenland gridbox 1 (figure 3). (*a*) Monthly and angular averaged values of $\chi_{n,a}$ for NOAA-9 are plotted versus time, with a least-squares linear fit shown for each month's data. The offsets among the linear fits are due to seasonal variability and to the different angular ranges used in different months ('bidirectional effects'). (*b*) The offsets are removed by iterative normalization of $\chi_{n,a}$ to that calender month's fitted value for January 1986, as described in the text (§5.2). The relative sensitivities are also adjusted for changes induced by orbital degradation (§5.1). The dashed line shows the value of dg/dt derived by ISCCP in their *absolute* calibration (see §1 of text), where we have also normalized the ISCCP data to January 1986 (Brest *et al.* 1997); the ISCCP results are nearly indistinguishable from our own.

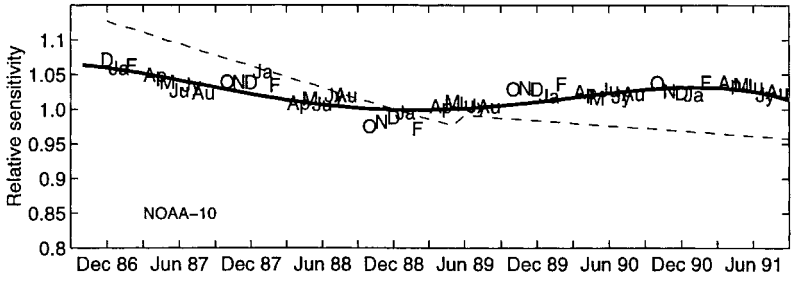

Figure 10. As in figure 9(*b*), but for NOAA-10.

drift in two ways: the trend line is fitted either before or after geographical averaging, and using the three different choices of maximum allowed θ_s. These six ways of computing drift could become eighteen ways if we also would permit three different ways of obtaining χ_n as discussed in §4.2 (mean, mean after cutoffs, or median), but the drift we derive is nearly identical for these three different ways of computing χ_n. The detrended standard deviation was slightly lower when the medians of χ

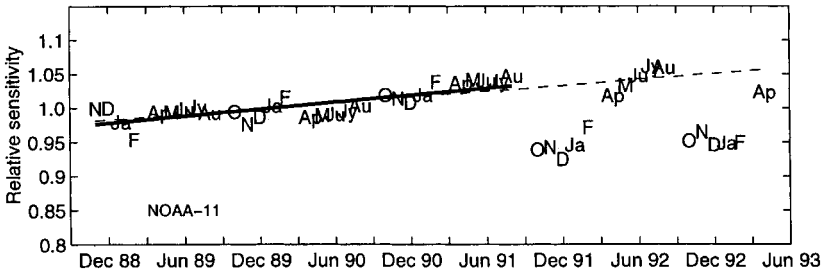

Figure 11. As in figure 9(*b*), but for NOAA-11. Data for November 1988 through July 1991 were used to generate the linear fits to the values of $\chi_{n,a}$; subsequent months were influenced by Pinatubo aerosols. All monthly averages, including months after July 1991, are normalized using the pre-Pinatubo data, but only pre-Pinatubo averages are included in the linear fit or in the calculation of drift uncertainty and detrended standard deviation.

distribution were used to calculate $\langle R \rangle_n$ values, as was the geographic variability, so we favour this approach for determination of calibration drift.

Finally, for NOAA-9 and NOAA-11 we also calculated calibration drift on a monthly basis. Values of $\chi_{n,a}$ from all gridboxes (in Antarctica for October–February and Greenland for April–August) were averaged together for a given month and year. A single linear fit was generated to the monthly data, yielding ten values of dg/dt. We did this to show that the adjustments we apply to the full dataset in the process described above do not falsely alter the derived change in calibration. What we see is that the combined dataset produces results that are in good agreement with the monthly-derived drift rates (table 3) but that the derived drift rates from the combined dataset have a much smaller uncertainty.

5.3. *Results*

NOAA-9. The calibration drift dg/dt, drift uncertainty, and detrended standard deviation we derive for NOAA-9 are insensitive to the angular range of bins chosen

Table 3. Derived calibration drift, calculated using only one month of data at a time. The values of $\chi_{n,a}$ are averaged over all geographic gridboxes and a single calibration drift rate is derived for each month.

	Drift (%/yr)	
Month	NOAA-9	NOAA-11
January	−5.22	+2.71
February	−4.74	+3.31
April	−5.46	+1.75
May	−4.98	+1.75
June	−5.46	+0.91
July	−4.86	+0.67
August	−3.90	+1.03
October	−4.86	+2.11
November	−5.82	+0.55
December	−5.46	+0.79
average ± standard deviation:	−5.08 ± 0.5	+1.56 ± 0.9

to calculate $\chi_{n,a}$ (table 4). The results for Method 1 and Method 2 are also very similar. We conclude that the gain of the NOAA-9 visible channel declined at a rate of $5.3 \pm 0.1\%$/year. In all cases $\sigma_d \leqslant 1.0\%$, indicating that dg/dt is nearly constant and that interannual variability in the monthly average bidirectional reflectance of the sub-ozone layer is quite small for all three ranges of (μ_s, μ_r) space used in the analysis.

NOAA-10. The NOAA-10 results are also consistent across all three cases of angular bin restrictions and between the two methods (table 4 and figure 10). A fourth-order polynomial appears to fit the dataset quite well, with $\sigma_d \leqslant 2.0\%$ in all cases. Our derived calibration using $\mu_s \geqslant 0.20$ with Method 2 yielded this polynomial fit for the relative gains:

$$g(t)/g(t_0) = 1.0656 - 6.19 \times 10^{-4} t - 2.86 \times 10^{-4} t^2 + 1.08 \times 10^{-5} t^3 - 1.02 \times 10^{-7} t^4 \quad (10)$$

where t is the time in months since November 1986 and t_0 is November 1988. The uncertainties in the coefficients are, respectively: ± 0.0078, $\pm 1.65 \times 10^{-4}$, $\pm 1.05 \times 10^{-4}$, $\pm 0.25 \times 10^{-5}$, and $\pm 0.20 \times 10^{-7}$.

It seems strange that the NOAA-10 detector sensitivity should decline for nearly two years and then start to increase. This change in dg/dt from negative to positive occurred at the same time that the afternoon satellite changed from NOAA-9 to NOAA-11, which may offer a clue. However, radiances used in this study were from the ISCCP nominal calibration dataset, meaning that only the pre-flight calibration coefficients (converting counts to radiances) should have been applied. Communication with ISCCP and AVHRR personnel confirmed that these radiances

Table 4. Derived calibration drift for NOAA-9 and 11 and detrended standard deviation for NOAA-9, 10 and 11. Values of $\chi_{n,a}$ were calculated for three different limits on solar zenith angle. In addition, calibration drift and detrended standard deviation, σ_d, were calculated using two methods, fitting the trend line either before (Method 2) or after (Method 1) geographical averaging. In Method 1, drift and σ_d are calculated for each pairing of Antarctic and Greenland geographic gridboxes with data in all months ('#box-pairs'). The average ($drift_g$) and standard deviation ($\sigma_{drift,g}$) over all gridbox pairs is shown in the column 'drift(%/yr)' as $drift_g \pm \sigma_{drift,g}$. The value of σ_d is the average value of σ_d for all gridbox pairs. In Method 2, monthly $\chi_{n,a}$ values are averaged over all gridbox pairs, and a single drift value is derived for the full dataset. The value of σ_d given is for the single fit.

		drift(%/yr)			σ_d(%)		
	Method	$\mu_s \geqslant 0.10$	$\mu_s \geqslant 0.15$	$\mu_s \geqslant 0.20$	$\mu_s \geqslant 0.10$	$\mu_s \geqslant 0.15$	$\mu_s \geqslant 0.20$
NOAA-9	1	-5.26 ± 0.13	-5.27 ± 0.14	-5.27 ± 0.13	1.03	1.00	0.92
	2	-5.26	-5.26	-5.27	0.80	0.82	0.73
#box-pairs		64	46	22	64	46	22
NOAA-10	1	—	—	—	1.87	1.49	1.43
	2	—	—	—	1.72	1.31	1.25
#box-pairs		64	58	38	64	58	38
NOAA-11	1	$+1.57 \pm 0.84$	$+1.98 \pm 0.44$	$+2.15 \pm 0.20$	2.90	2.01	1.25
	2	$+1.39$	$+1.94$	$+2.28$	2.64	1.75	1.15
#box-pairs		64	40	22	64	40	22

have not been 'corrected' for inter-satellite calibration. Personnel at NOAA-NESDIS indicated that there may have been solar contamination for the NOAA-10 radiances starting around the time we see the detector sensitivity starting to increase, but this would be expected to affect c_0 more than g.

Our determination of calibration drift differs significantly from ISCCP's for the NOAA-10 sensor. The ISCCP calibration procedure assumes a linear change in calibration with time, which we do not. Also, the dashed line plotted in figure 10 shows dg/dt from ISCCP's *absolute* calibration tables, so a correction for inter-satellite calibration has been applied. The jump in relative sensitivity and change in the slope of the line in May 1989 may be the result of a switch from NOAA-9 to NOAA-11 as the normalization satellite.

NOAA-11. The NOAA-11 detector sensitivity increased with time, and a linear fit seems most appropriate. However, the derived value of dg/dt and its uncertainty, as well as σ_d, all were sensitive to the range of angular bins used (table 4). Inspection of the NOAA-11 χ functions revealed anomalous values of χ_n at large solar zenith angles (small μ_s), particularly in December. When data from small μ_s are rejected, the uncertainty of dg/dt and σ_d decrease notably.

There are three possible sources of these anomalies at large solar zenith angles. Changes in the actual sub-ozone bidirectional reflectance that are not accounted for in our model, non-linear changes in the sensitivity of the AVHRR detector, and/or inaccuracies in the AVHRR dataset could all affect the results. At large solar zenith angles $\chi_n(\theta_s, \theta_r, \phi)$ varies steeply with angle (figure 4), so small errors in the satellite zenith angle specified in the radiance dataset, for example, would lead to significant inaccuracies in our derived values of χ_n.

The consistently low interannual variability for NOAA-9 indicates that the model does an excellent job of accounting for month-to-month changes and geographical variation in the true bidirectional reflectance over the multi-year lifetime of a satellite instrument. The larger month-to-month variations seen for NOAA-11 are therefore unlikely to be caused by surface or cloud variability, and must be attributed to the satellite.

The scatter of points about the line on figure 9(*b*)is somewhat larger for August than for other months, perhaps due to a small amount of melting in parts of the Greenland gridboxes, as suggested by Nolin and Stroeve (1997), but the calculated drift is the same whether or not Greenland data are used.

The ISCCP calibration results show evidence of non-linear behaviour in NOAA-11 sensitivity that is not present for the NOAA-9 detector, as do our results when large solar zenith angles are included in the analysis. ISCCP's drift-corrected reflectance shows a jump between July and November of 1991 (Brest *et al.* 1997) and a subsequent decrease in reflectance that is likely due to the effects of Mt Pinatubo aerosols. However, several significant fluctuations in ISCCP's corrected reflectances occur before the eruption. These fluctuations are much larger than they found for NOAA-7 and NOAA-9 corrected data, indicating that the ISCCP calibration method may also be suffering from the same type of noise we see when using data from large solar zenith angles.

Because σ_d for NOAA-11 is lowest (1.2%) when we restrict ourselves to the angular range $\mu_s \geqslant 0.20$ and when we use Method 2, we choose this combination as giving the best estimation of calibration drift (table 4 and figure 11). We conclude that the NOAA-11 visible channel sensitivity *increased* at a rate of $2.3 \pm 0.2\%$/year, in good agreement with ISCCP's estimate of the drift (dashed line in figure 11). While it is unlikely that the photon-to-electron conversion efficiency of the optical

detector would increase with time, changes in the detector electronics or changes in the bandwidth of optical filters preceding the detector could lead to a positive value for dg/dt.

6. Recommendations for use of Antarctica and Greenland as visible channel calibration targets

The Antarctic and Greenland plateaus appear to be effective calibration targets for visible channels on satellites, as demonstrated by Loeb (1997) and herein using three of the AVHRR instruments. The size, spatial uniformity, and high albedo of the plateaus make them excellent natural calibration targets. Their successful use as calibration targets, however, depends on several key factors accounted for in our model.

First, as when using other ground-based targets for calibration (Brest and Rossow 1992, Che and Price 1992, Kaufman and Holben 1993, Rao and Chen 1995, Loeb 1997), bidirectional effects must be removed by binning the data by solar and satellite zenith angles. Here we also restrict the model to near-nadir satellite views. This is critical in the Antarctic because solar zenith angles are always large and $\chi(\theta_s, \theta_r, \phi)$ changes more rapidly with θ_r when θ_s is large.

Second, the analysis should be restricted to regions of low slope and high elevation. This minimizes noise in the model results, as is demonstrated by comparing the angle-averaged near-nadir geographic variability, $\sigma_{g,a}$, of the derived χ_n from low-slope, high elevation regions to that from high-slope, low elevation regions (figure 12). Even amongst the 32 low-slope, high elevation Antarctic gridboxes, we can see that the detrended standard deviation, σ_d, is lower in the interior of the plateau than at the margins (figure 13).

Third, Chappuis-band absorption should be accounted for using the local daily value of total column ozone amount, rather than a fixed climatological value. This

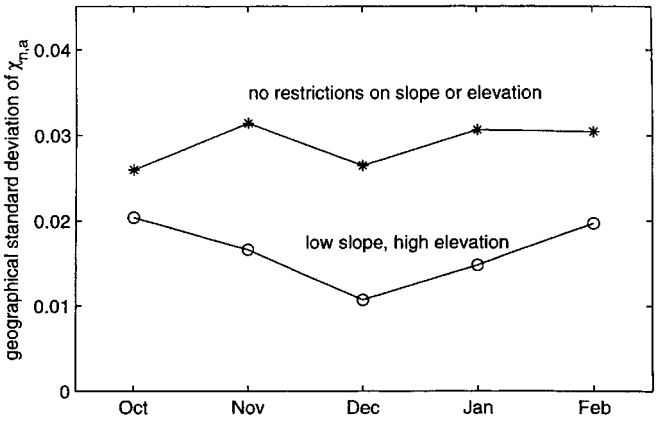

Figure 12. Angular average geographic variability, $\sigma_{g,a}$, of near-nadir derived values of χ_n for the 1985–86 season over 32 low-slope/high elevation Antarctic gridboxes where pixels with slope greater than 0.006 radians or elevation less than 2 km were excluded (○), and among 28 gridboxes, most of which contain high-slope or low elevation regions, where no slope restriction was imposed and the elevation was required only to exceed 50 m (1). In both cases, the average is taken only over angular bins with $\mu_r \geqslant 0.95$ and $\mu_s \geqslant 0.10$. The high-slope/low elevation gridboxes are predominantly located near the perimeter of Antarctica.

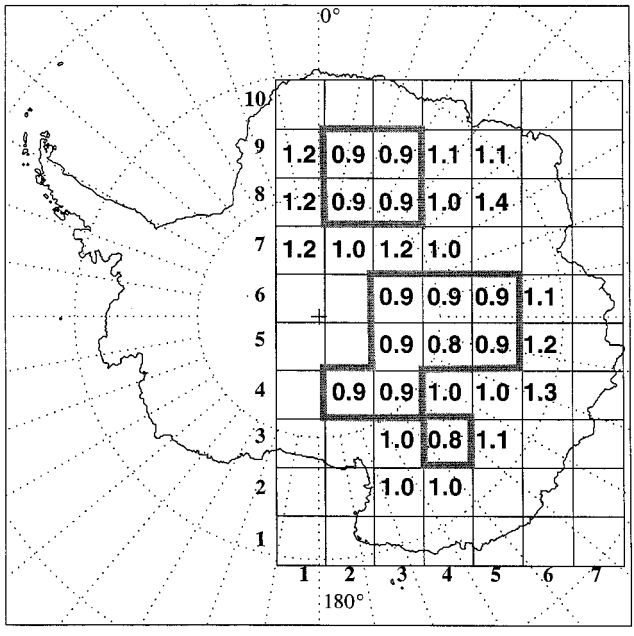

Figure 13. The detrended standard deviation, σ_d, in percent, of drift values for NOAA-9, for the 32 Antarctic gridboxes used in the model. Note that those gridboxes with $\sigma_d < 1.0\%$, outlined in a heavy border, are generally located on the central portion of the high plateau.

is particularly critical during the months of October and November for Antarctica and April and May for Greenland, when the ozone amount is most variable. Interannual changes in the average total column ozone for a given month of the year will add error to the model-derived calibration drift. For example, in years with more ozone there will be more Chappuis-band absorption, so the radiances seen by the AVHRR will be darker and, if changing ozone amount is not accounted for, the derived value of χ would be smaller.

To demonstrate this effect, we generated χ functions for the months of October to February over Antarctica for the full lifetime of the NOAA-9 AVHRR using a fixed total column ozone amount of 300 Dobson Units. The angular average geographic variability, $\sigma_{g,a}$, of χ calculated using fixed total column ozone amount was $\sim 20\%$ greater than for the χ_n functions generated using local daily ozone amounts from TOMS.

Calibration drift and detrended standard deviation were also calculated from the Antarctic data only, using χ_n obtained using TOMS daily ozone, then again using χ_n assuming fixed total column ozone. The value of σ_d, averaged over the 32 geographic gridboxes, increased from 1.2% to 1.9%, and the derived calibration drift changed from $(-5.4 \pm 0.3)\%$/year to $(-6.2 \pm 0.3)\%$/year. While increased σ_d is to be expected when TOMS data are replaced with a fixed column ozone amount, the significant increase in derived calibration drift is somewhat surprising. The reason for the change can be seen by inspection of figure 14, which shows the detrended relative gain derived for channel 1. The dramatic fluctuation in the October mean total column ozone from 1986 to 1988 is accompanied by an interannual change in derived relative gain. The derived gain for October 1988 is much lower than it would have been if the true total column ozone had been accounted for. Since October is

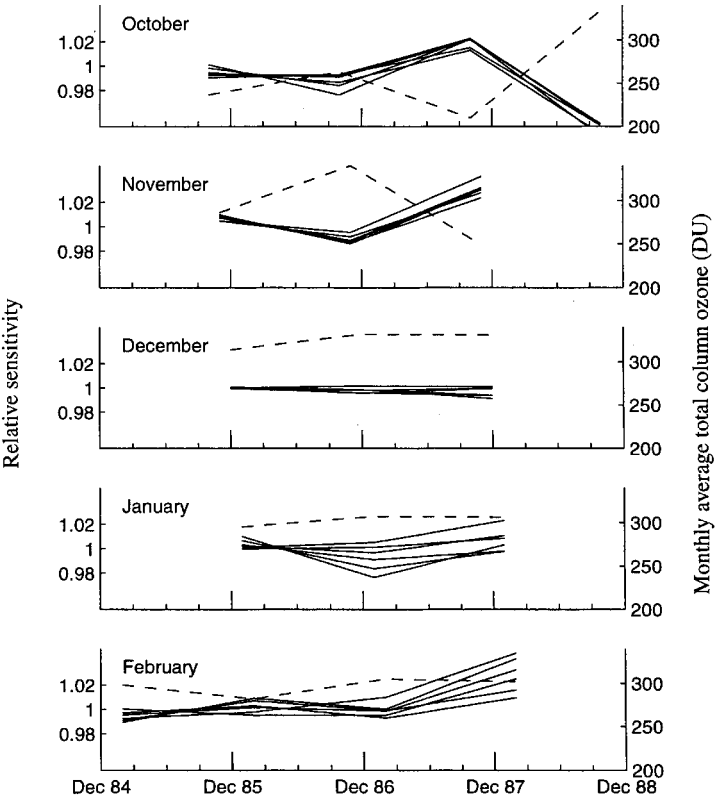

Figure 14. The effect of not accounting for variable total column ozone over Antarctica. Monthly average total column ozone in Dobson Units (DU) for a given month of the year (dashed line) are plotted, along with the detrended (by 5.3% per year; see text) relative gain for the same month for six geographic gridboxes (solid lines). The values would all be very close to 1.0 if local daily values of total ozone had been used. Deviations from 1.0 correlate well with interannual changes in mean total column ozone, particularly in October and November, the months of most variable ozone. The gridboxes used here are (3,5), (3,6), (3,7), (4,5), (4,6) and (4,7), as defined by the coordinate system in figure 3(*a*).

the only data point available for the second half of 1988, it has a strong influence in determining the slope of the linear fit to the full datset for all months.

If daily ozone amounts are not available from TOMS or a similar instrument, then the determination of drift should probably include Antarctic data only for December, as in Loeb's (1997) study, because ozone is less variable in that month and the Sun is higher so Chappuis-band absorption is less. Climatological values of total column ozone could also be used if the ozone hole is reliably the same in successive years, or if a correction to the climatology is applied to account for changes in ozone. Non-absorbing aerosols below the ozone layer should not affect the determination of channel 1 calibration drift, but aerosols within or above the ozone layer can be troublesome, as seen in 1992 for NOAA-11.

7. Conclusion

The visible channels of AVHRR instruments exhibits large drifts in their gain. Since these channels are used for climate monitoring, it is important to develop

methods to track the gain accurately. The drift is sometimes very steady, as for NOAA-9, but for NOAA-11 it is noisier and for NOAA-10 it is not even monotonic. It is therefore valuable to have estimates of the gain at monthly intervals.

We can recommend the snow surfaces of the high plateaus of Greenland and Antarctica as calibration targets that can be used ten months of the year for visible and near-ultraviolet channels. Snow is less suitable as a calibration for near-infrared channels, because in the near-IR its albedo is sensitive to day-to-day changes in surface grain size; however, Loeb (1997) and Tahnk and Coakley (2001) have been successful in using snow to calibrate channel 2. These polar snow surfaces are seen every day by polar-orbiting satellites, and have several other advantages over desert surfaces. Even satellites that have on-board calibration for shortwave channels would benefit from a secondary calibration method as a check of the on-board calibration.

The drifts we derive are robust, in that they are insensitive to the choice of gridboxes on the Antarctic Plateau, to the choice of months, and to the incorporation of cloud-rejection schemes.

Acknowledgments

The AVHRR data used in this research were obtained from the EOSDIS Distributed Active Archive Center at the NASA Langley Research Center. We thank Jonathan Bamber for providing the slope and elevation data for Antarctica, Richard Stephenson for providing his program to calculate solar zenith and azimuth, and Robert Boime, Normal Loeb, Glen Jaross, Arlin Krueger and Konrad Steffen for discussions. This work was supported by NASA grant NAG5-3779.

References

Anderson, S. M., and Mauersberger, K., 1992, Laser measurements of ozone absorption cross sections in the Chappuis band. *Geophysical Research Letters*, **19**, 933–936.

Bader, H., 1961, CRREL Report I-B2. Cold Regions Research and Engineering Laboratory, Hanover, New Hampshire, 18 pp.

Bamber, J. L., 1994, A digital elevation model of the Antarctic ice sheet derived from ERS-1 altimeter data and comparison with terrestrial measurements. *Annals of Glaciology*, **20**, 48–54.

Boime, R., and Warren, S. G., 1993, Mapping Antarctic ozone from visible-channel data. *Proceedings SPIE*, **2047**, *Atmospheric Ozone*, 122–131.

Brest, C. L., and Rossow, W. B., 1992, Radiometric calibration and monitoring of NOAA AVHRR data for ISCCP. *International Journal of Remote Sensing*, **13**, 235–273.

Brest, C. L., Rossow, W. B., and Roiter, M. D., 1997, Update of radiance calibration for ISCCP. *Journal of Atmospheric and Oceanic Technology*, **14**, 1091–1109.

Che, N., and Price, J. C., 1992, Survey of radiometric calibration results and methods for visible and near-infrared channels of NOAA-7, -9 and -11 AVHRRs. *Remote Sensing of Environment*, **41**, 19–27.

Deshler, T., Johnson, B. J., and Rozier, W. R., 1994, Changes in the character of polar stratospheric clouds over Antarctica in 1992 due to the Pinatubo volcanic aerosol. *Geophysical Research Letters*, **21**, 273–276.

Doherty, S. J., 1997, The Snow Surface of the Antarctic Ice Sheet as a Calibration Target for Visible and UV Channels on Satellites. MS Thesis, University of Washington, Seattle, 88 pp.

Dozier, J., and Frew, J., 1989, Rapid calculation of terrain parameters for radiation modelling from digital elevation data. *Proceedings IGARSS*, *IEEE Transactions on Geoscience and Remote Sensing*, 1769–1774.

Gow, A. J., 1965, On the accumulation and seasonal stratification of snow at the South Pole. *Journal of Glaciology*, **5**, 467–477.

Grenfell, T. C., Warren, S. G., and Mullen, P. C., 1994, Reflection of solar radiation by the

Antarctic snow surface at ultraviolet, visible and near-infrared wavelengths. *Journal of Geophysical Research*, **99**, 18 669–18 684.

Jaross, G., 1993, Ice radiance method for BUV instrument monitoring. *Proceedings SPIE*, **2047**, *Atmospheric Ozone*, 94–101.

Kaufman, Y. J., and Holben, B. N., 1993, Calibration of the AVHRR visible and near-IR bands by atmospheric scattering, ocean glint and desert reflection. *International Journal of Remote Sensing*, **14**, 21–52.

Leu, D. J., 1977, Visible and near-infrared reflectance on beach sands. A study of the spectral reflectance/grain size relationship. *Remote Sensing of Environment*, **6**, 169–182.

Loeb, N. G., 1997, In-flight calibration of NOAA AVHRR visible and near-IR bands over Greenland and Antarctica. *International Journal of Remote Sensing*, **18**, 477–490.

McCormick, M. P., and Trepte, C. R., 1987, Polar stratospheric cloud optical depth observed between 1978 and 1985. *Journal of Geophysical Research*, **92**, 4297–4306.

Nolin, A. W., and Stroeve, J., 1997, The changing albedo of the Greenland ice sheet: implications for climate modelling. *Annals of Glaciology*, **25**, 51–57.

Ohring, G., and Booth, A. L., 1995, The NOAA pathfinder program. *Advances in Space Research*, **16**, 15–20.

Parish, T. R., and Bromwich, D. H., 1987, The surface windfield over the Antarctic ice sheets. *Nature*, **328**, 51–54.

Poole, L. R., and Pitts, M. C., 1994, Polar stratospheric cloud climatology based on Stratospheric Aerosol Measurement II observations from 1978 to 1989. *Journal of Geophysical Research*, **99**, 13 083–13 089.

Rao, C. R. N., and Chen, J., 1995, Inter-satellite calibration linkages for the visible and near-infrared channels of the Advanced Very High Reoslution Radiometer on the NOAA-7, -9 and -11 spacecraft. *International Journal of Remote Sensing*, **16**, 1931–1942.

Rao, C. R. N., and Chen, J., 1996, Post-launch calibration of the visible and near-infrared channels of the Advanced Very High Resolution Radiometer on the NOAA-14 spacecraft. *International Journal of Remote Sensing*, **17**, 2743–2747.

Rossow, W. B., and Schiffer, R. A., 1991, ISCCP cloud data products. *Bulletin of the American Meteorological Society*, **72**, 2–20.

Rossow, W. B., Desormeaux, Y., Brest, C. L., and Walker, A., 1992, International Satellite Cloud Climatology Project (ISCCP) Radiance Calibration Report. WMO/TD-No. 520, WCRP-77, World Meteorological Organization, 104 pp.

Rossow, W. B., Walker, A., and Roiter, M., 1996, International Satellite Cloud Climatology Project (ISCCP) Description of Reduced Resolution Radiance Data. WMO/TD-No. 58. World Meteorological Organization, 163 pp.

Seko, K., Furukawa, T., Nishio, F., and Watanabe, O., 1993, Undulating topography on the Antarctic ice sheet revealed by NOAA AVHRR images. *Annals of Glaciology*, **17**, 55–62.

Staylor, W. F., 1990, Degradation rates of the AVHRR visible channel for the NOAA-6, -7 and -9 spacecraft. *Journal of Atmospheric and Oceanic Technology*, **7**, 411–423.

Suttles, J. T., Green, R. N., Minnis, P., Smith, G. L., Staylor, W. F., Wielicki, B. A., Walker, I. J., Young, D. F., Taylor, V. R., and Stowe, L. L., 1988, *Angular Radiation Models for Earth-atmosphere System*, Vol. 1, Shortwave Radiation, *NASA Ref. Pub. 1184*, National Aeronautics and Space Admin., Washington, D.C.

Tahnk, W. R., and Coakley Jr., J. A., 2001, Improved calibration coefficients for NOAA-14 AVHRR visible and near-IR channels. *International Journal of Remote Sensing*, 1269–1283.

Vigroux, E., 1953, Contribution a l'étude experimentale de l'absorption de l'ozone. *Annales de Physique*, **8**, 709–762.

Warren, S. G., Brandt, R. E., and O'Rawe Hinton, P., 1998, Effect of surface roughness on bidirectional reflectance of Antarctic snow. *Journal of Geophysical Research*, **103**, 25 789–25 807.

Warren, S. G., Hahn, C. J., London, J., Chervin, R. M., and Jenne, R. L., 1986, Global Distribution of Total Cloud Cover and Cloud Type Amounts Over Land. NCAR/TN-273 + STR, National Center for Atmospheric Research, Boulder, CO.

Wiscombe, W. J., and Warren, S. G., 1980, A model for the spectral albedo of snow, I: Pure snow. *Journal of Atmospheric Sciences*, **37**, 2712–2733.

Wiscombe, W. J., Welch, R. M., and Hall, W. D., 1984, The effects of very large drops on cloud absorption. Part I: Parcel models. *Journal of Atmospheric Sciences*, **41**, 1336–1355.

Wu, A., and Zhong, Q., 1994, A method for determining the sensor degradation rates of NOAA AVHRR Channels 1 and 2. *Journal of Applied Meteorology*, **33**, 118–122.